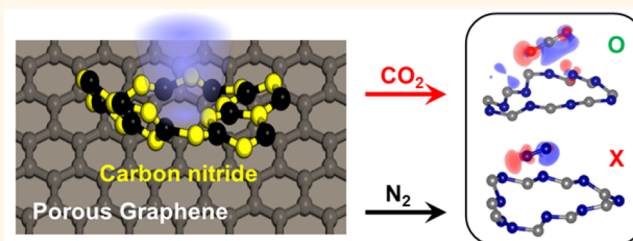# Selective and Regenerative Carbon Dioxide Capture by Highly Polarizing Porous Carbon Nitride

Youngtak Oh,[†,‡,#] Viet-Duc Le,[§,#] Uday Narayan Maiti,[‡] Jin Ok Hwang,[‡] Woo Jin Park,[⊥] Joonwon Lim,[†,‡] Kyung Eun Lee,[†,‡] Youn-Sang Bae,[∥] Yong-Hyun Kim,[*,§] and Sang Ouk Kim[*,†,‡]

[†]National Creative Research Initiative Center for Multi-Dimensional Directed Nanoscale Assembly, [‡]Department of Material Science and Engineering, [§]Graduate School of Nanoscience and Technology, and [⊥]Department of Chemistry, KAIST, Daejeon 34141, Korea and [∥]Department of Chemical and Biomolecular Engineering, Yonsei University, Seoul 120-749, Korea. [#]Y.O. and V.-D.L. contributed equally.

ABSTRACT Energy-efficient CO_2 capture is a stringent demand for green and sustainable energy supply. Strong adsorption is desirable for high capacity and selective capture at ambient conditions but unfavorable for regeneration of adsorbents by a simple pressure control process. Here we present highly regenerative and selective CO_2 capture by carbon nitride functionalized porous reduced graphene oxide aerogel surface. The resultant structure demonstrates large CO_2 adsorption capacity at ambient conditions

Selective CO_2 capture *via* dipole induced-dipole Interaction

(0.43 mmol·g^{-1}) and high CO_2 selectivity against N_2 yet retains regenerability to desorb 98% CO_2 by simple pressure swing. First-principles thermodynamics calculations revealed that microporous edges of graphitic carbon nitride offer the optimal CO_2 adsorption by induced dipole interaction and allows excellent CO_2 selectivity as well as facile regenerability. This work identifies a customized route to reversible gas capture using metal-free, two-dimensional carbonaceous materials, which can be extended to other useful applications.

KEYWORDS: carbon nitride · graphene · aerogel · CO_2 capture · density functional theory

Post-combustion gas from power plants, namely flue gas, accounts over 40% of all CO_2 emissions. Effective management of flue gas is of colossal research interest as a sustainable energy supply and remediation of global climate change.[1] Presently, industrial flue gas control is principally based on wet chemical absorption using alkanolamine solvents.[2] Unfortunately, separation of CO_2 and regeneration of these solvents require intensive amount of energy (up to 30% of total energy production).[3] Moreover, the corrosive operating condition raises significant maintenance cost.[4,5] Various porous solid adsorbents have been proposed as alternatives, including zeolites[6,7] and metal organic framework (MOFs).[8−13] Those solid adsorbents relying on the high isosteric adsorption of metallic components ($E_{ads} \sim 0.4-1.0$ eV) may attain remarkably high volumetric CO_2 capacity and selectivity but commonly suffer from hard regenerability of the adsorbents and subtle sensitivity to ambient humidity.[14]

An ideal CO_2 adsorbent should bear appropriate adsorption energy that can counterbalance the adsorption capacity and the regenerability for easy CO_2 capture/release system. A recent systematic DFT study has shown that CO_2 affinity of MOF-74 can be tuned from 0.3 to 0.5 eV, depending on nature of the building unit.[15] The hydroxyl group, if present in MOF, can also anchor oxygen terminals of CO_2 *via* hydrogen bonds.[16] Strong orbital coupling between CO_2 and adsorbent can result in noticeable bending of CO_2 and an adsorption energy as high as 0.7 eV.[17] In this regard, adsorbents with intermediate adsorption energy without strong perturbation of electronic structures of CO_2 and adsorbents are expected to satisfy the subtle requirements for large capacity/selectivity along with easy regeneration.

Here, we introduce the unique concept of effective CO_2 capture system under ambient temperature and pressure, and highly selective adsorption against N_2 through polarizing nitrogen edges of carbon nitride

pore sites. Graphitic carbon nitride (g-C$_3$N$_4$) is a layered material consisting of hexagonally organized heptazine (tri-s-triazine) units linked by tertiary amines.[18] Its nonplanar structure with well-defined porosity (pore diameter $d = 0.75$ nm) results from the buckled packing of heptazine chain. Intrinsic semiconducting property (optical band gap ~2.7 eV), chemical/thermal stability, and genuine microporosity of the carbon nitride have been exploited for metal-free photocatalyst, biomolecule imaging, and so on.[19−23] However, currently available synthetic methods yield a highly condensed form of carbon nitride with minimal surface area.[24,25] Tight interlayer packing between heptazine units prevent exploitation of the potential large surface area of the carbon nitride, and conventional exfoliation techniques are not as efficient as other two-dimensional materials.[26,27] For this reason, applications requiring genuine large surface of carbon nitride (*e.g.*, CO$_2$ capture) have been rarely shown. To overcome this problem, we chose the reduced graphene oxide aerogel surface to provide desirable porous structure and template platform to grow carbon nitride on the surface. Subsequent procedures of gelation of graphene oxide solution with soluble carbon nitride precursor (Dicyandiamide), solvent exchange, liquid extraction, and thermal treatment in the nitrogen results in highly porous reduced graphene oxide aerogel network composed of carbon nitride moieties. This heterostructure inherits large adsorption capacity and selectivity, but eliminates high isosteric adsorption energy. Induced dipole−dipole interactions highly specific for CO$_2$ molecules at the porous carbon nitride surface, whose strength is larger than typical physisorption (0.01−0.1 eV), achieve excellent regenerability ($R = 97.6\%$) of adsorbent along with decent CO$_2$ adsorption capacity (0.43 mmol·g^{-1} at 0.1 bar, 300 K) and high selectivity ($\alpha12^{ads} = 427$).

RESULTS AND DISCUSSION

Synthesis and Characterization of Carbon Nitride Functionalized Reduced Graphene Oxide Aerogel. Figure 1 presents a
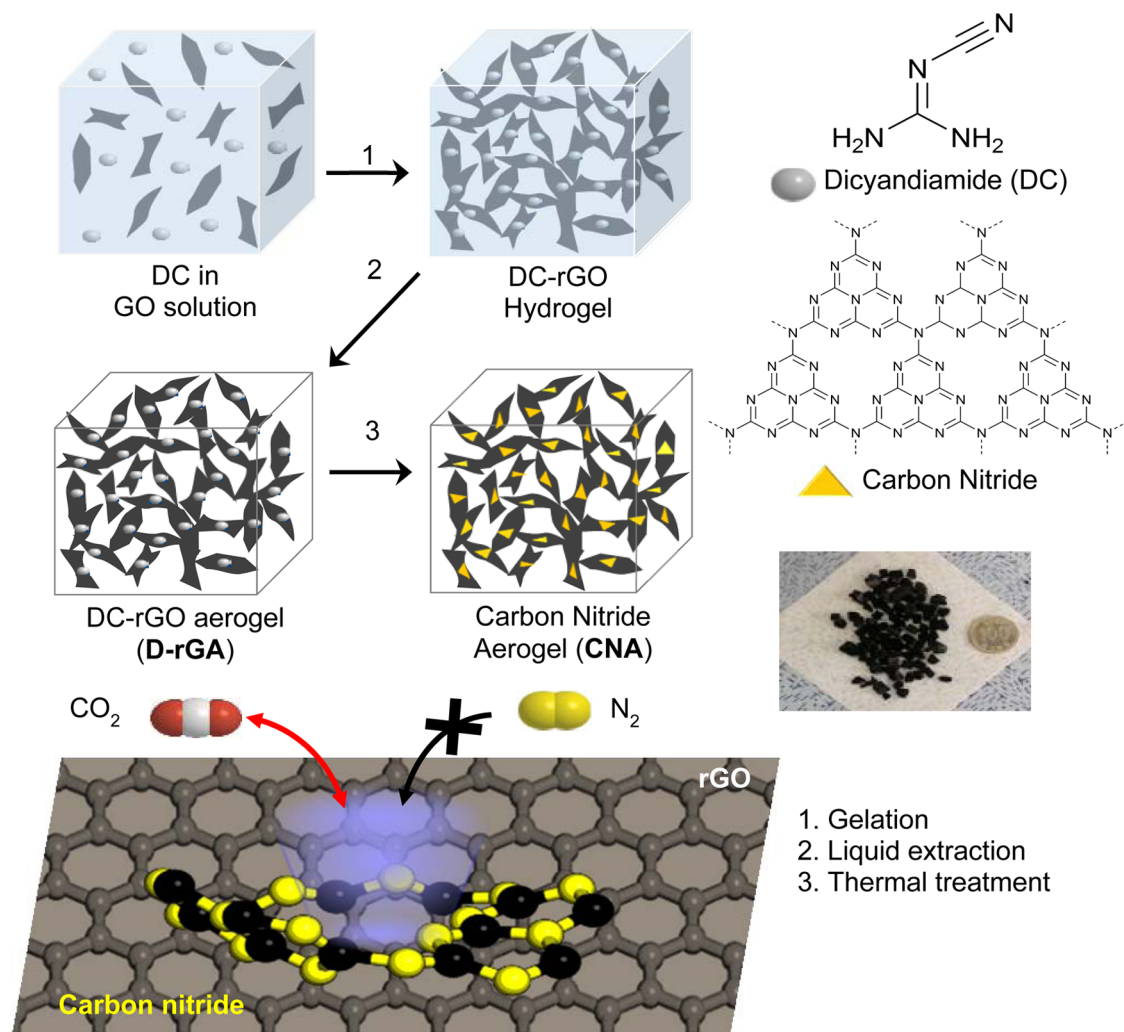
Figure 1. Synthetic procedure for carbon nitride aerogel (CNA). Modified sol−gel reduction of graphene oxide (GO) with dicyandiamide resulted in dicyandiamide-functionalized reduced graphene oxide (DC-rGO) hydrogel. Subsequent liquid extraction with supercritical CO$_2$ drying and thermal treatment transform this hydrogel into carbon nitride embedded graphene aerogel, which is capable of selective CO$_2$ gas capture against N$_2$.

synthetic approach to construct carbon nitride functionalized reduced graphene oxide aerogel (CNA). Dicyandiamide, a soluble precursor of carbon nitride, is cross-linked into the gel structure in the presence of a porous graphene network, which was prepared by mild reduction of exfoliated graphene oxide aqueous dispersion.[15] During the gelation process, oxygen functional groups (carboxyl, phenolic, carbonyl, hydroxyl) of graphene oxide facilitate cross-linking with amine groups of dicyandiamide providing a subtle platform for carbon nitride growth.[28] Carbon nitride is grown by subsequent procedures of solvent exchange, liquid extraction, and thermal treatment. These processes remove soluble impurities, extract water molecules trapped within graphene layers while preserving porous network, and transform dicyandiamide precursors at the graphene surface into the two-dimensional carbon nitride phase. A highly porous structure composed of carbon nitride moieties is constructed based on this scalable sol−gel route with inexpensive metal-free carbonaceous precursors. This bottom-up synthetic strategy exploits adequately soluble dicyandiamide as the building block of carbon nitride and the graphene surface as the robust porous framework which maintains its skeletal structure during the thermal growth of carbon nitride. Given the low solubility and dispersibility of carbon nitride, conventional exfoliation and nanostructuring techniques are not a viable option to yield a homogeneous carbon nitride/graphene system.

One of the most critical criteria for effective solid adsorbent is robust porous structure that grants high surface area and facile permeation/diffusion of adsorbate. Porous structure of CNA is carefully analyzed by porosimetric measurements based on N_2 and Ar isotherms, which present that graphene gelation and critical point drying are essential steps for desirable porous structure. N_2 adsorption isotherm (Supporting Information, S Figure 1) represents a type II isotherm with initial adsorption at low partial pressure region ($P/P_0 < 0.01$) followed by gradual adsorption at intermediate region ($0.01 < P/P_0 < 0.8$) and rapid adsorption at the saturation pressure region ($P/P_0 > 0.8$) with large surface area (450 $m^2 \cdot g^{-1}$), large pore volume (1.5 $cm^3 \cdot g^{-1}$), and a considerable amount of meso- ($2 < d < 50$ nm) and macropores ($d > 50$ nm). The Argon (Ar) adsorption isotherm offers complementary information for well-defined micropores (Figure 2a). Pore
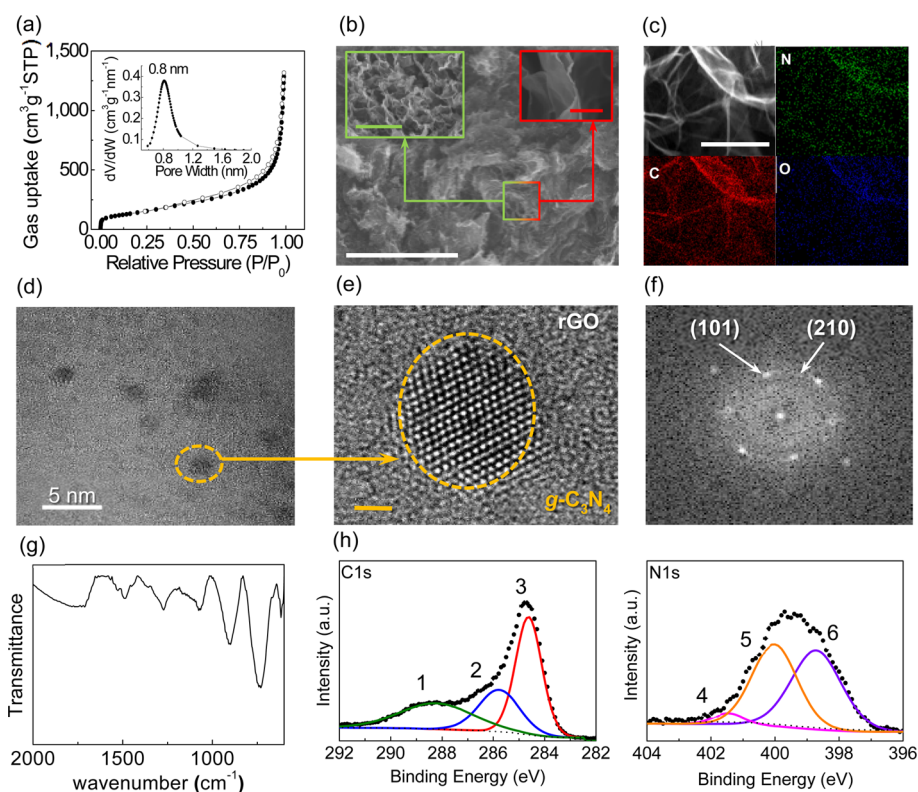
Figure 2. Porous structure and spectroscopic characterizations of CNA. (a) Ar adsorption isotherm and pore size distribution (inset). (b) Scanning electron microscope (SEM) analysis of CNA. White, green, and red scale bars represent 100 μm, 2 μm, and 2 nm, respectively. (c) Scanning transmission electron microscope (STEM) image and elemental mapping. Scale bar is 400 nm. (d) High-resolution transmission electron microscope (HR-TEM) of CNA and (e) crystalline domains of g-C_3N_4 on reduced graphene oxide (rGO) surface. Scale bar represents approximately 1 nm. (f) Discrete phase of g-C_3N_4 in (101) and (210) orientation from corresponding area of (e). (g) Attenuated total reflectance infrared (ATR-IR) spectroscope. (h) X-ray photoelectron spectroscopy (XPS) analysis. Deconvoluted peaks represent graphene oxide domains (1), C−N bonding (2), graphitic sp^2 carbon (3), tertiary nitrogen bound to three carbons (4), terminal amine defect site (5), and aromatic C=N−C domains from carbon nitride (6), respectively.

size distribution based on the Horvath−Kawazoe model detects 0.8 nm micropores, which corresponds to the cavity space of buckling heptazine units (inset of Figure 2a). More in-depth analysis of this pore site and its impact on the high selectivity toward CO_2 are given in the computational study section below.

Morphology of CNA is visualized by scanning electron microscope (SEM) (Figure 2b). Macroporous spongy-looking channels (Figure 2b and green inset) composed of graphene layers (Figure 2b red inset) are observed. During the gelation from graphene oxide dispersion, the pores originate from the space once occupied by the water molecules trapped within graphene oxide layers. Individual reduced graphene oxide flakes possess average layer thickness of 2.1−2.5 nm (Supporting Information, S Figure 2). The macroscopic structure of CNA features a highly amorphous surface of reduced graphene oxide framework as shown in the PXRD pattern (Supporting Information, S Figure 3). Elemental mapping by scanning transmission electron microscope (STEM) reveals the fairly well-dispersed nitrogen, carbon, and oxygen elements throughout the specimen (Figure 2c). During the thermal treatment of D-rGA, discrete carbon nitride phases are gradually grown on the porous graphene surfaces (CNA), as demonstrated by a high-resolution transmission electron microscope (HR-TEM) (Figure 2d,e and Supporting Information, S Figure 4). The apparent domains of g-C_3N_4 are well-dispersed throughout the reduced graphene oxide (rGO) surface, some of which show a discrete diffraction pattern of specific lattice direction (Figure 2f). This direct visualization of carbon nitride domains confirms the successful heterostructure of carbon nitride on the porous carbon surface.

A series of complementary analyses are conducted to understand the macroscopic and local structure of CNA, including attenuated total reflectance infrared (ATR-IR) and X-ray photoelectron spectroscopy (XPS). Various IR bands of CNA reflect the presence of carbon nitride functional groups (Figure 2g and Supporting Information, S Table 1). The development of aromatic C−N bonding (1450−1600 cm^{-1}) and skeletal vibration of tri-s-triazine (730−740 cm^{-1}) after thermal treatment indicate the growth of carbon nitride on

graphene gel.[26,29−31] XPS analysis shows the deconvoluted peaks of carbon nitride at 285−288 eV (peak 2), 398−399 eV (peak 6), 399.5−400.5 eV (peak 5), and 401−402 eV (peak 4), which correspond to C−N, aromatic C=N−C, aliphatic C=N (or N−H), and tertiary amine bound carbon, respectively (Figure 2h and Supporting Information, S Figure 5).[32−37] The peaks at 297−291 eV (peak 1) and 284.5 eV (peak 3) responds to oxidized and pristine graphitic carbon domains of reduced graphene oxide, respectively. Evolution of the XPS peaks during thermal annealing (25−600 °C) confirms the condensation of dicyandiamide into polymeric carbon nitrides as well as the presence of functional groups from reduced graphene oxide template. Notably, successful formation of carbon nitride at temperatures significantly lower than usual condensation temperature (500−600 °C) is induced by reduced graphene oxide templates. As demonstrated by Oh et al., graphene oxide functions as catalytic surface to grow carbon nitride even at 100 °C.[38] Excessive thermal treatment at higher temperatures ($T > 400$ °C) leads to the substantial loss of surface area that ultimately hampers overall CO_2 capture functionality (Supporting Information, S Figure 6). Elemental analysis through CHN pyrolysis and XPS reveals that CNA sample contains as much as 8 wt % of nitrogen (~13 wt % of carbon nitride).

CO_2 Capture Evaluation of CNA and Benchmark Materials. The efficient CO_2 capture behavior of CNA is demonstrated through CO_2 adsorption analysis along with dicyandiamide-functionalized reduced graphene oxide aerogel (D-rGA) and pristine reduced graphene oxide aerogel (rGA) as shown in Figure 3a. rGA shows 0.9 mmol·g^{-1} adsorption capacity at standard ambient temperature and pressure (SATP: $T = 300$ K and $P = 1$ bar), whereas D-rGA shows enhanced CO_2 uptakes of 2.2 mmol·g^{-1} at SATP. Subsequent thermal annealing at 200 °C under N_2 atmosphere condenses dicyandiamides to polymeric carbon nitrides, which further enhance CO_2 adsorption capacity up to 4.2 mmol·g^{-1} at SATP. All adsorption capacity is evaluated on the basis of the total weight of the sample.

To grasp CO_2 capture capability of CNA, CO_2 adsorption capacity (N_1^{ads}), working capacity (ΔN_1),
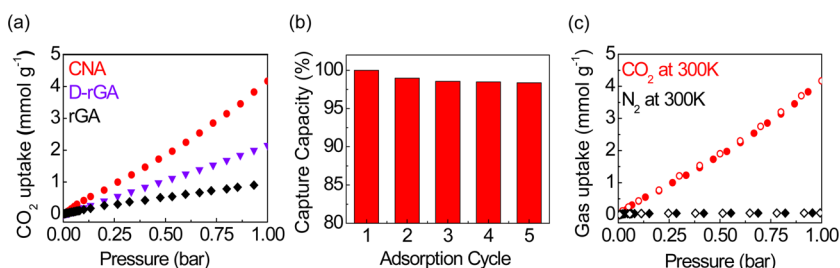
Figure 3. (a) CO_2 adsorption isotherms of carbon nitride aerogel (CNA), dicyandiamide-functionalized reduced graphene oxide aerogel (D-rGA), and pristine reduced graphene oxide aerogel (rGA). (b) Multiple cycles of relative CO_2 adsorption capacity for regenerability test for CNA at 1 bar. (c) CO_2 and N_2 adsorption isotherms of CNA with high selectivity toward CO_2.

TABLE 1. CO$_2$ Adsorbent Evaluation Results of Selected Benchmark Materials and CNA for Vacuum Swing Adsorption Process (VSA)^a

adsorption of CO$_2$ at 300 K	N_1^{ads}	ΔN_1	R	α_{12}^{ads}	S
ZIF-78[65]	0.60	0.58	96	35	396
Zeolite-5A[6]	3.50	2.36	67	62	163
Zeolite-13X[7]	2.49	1.35	54	86	128
Ni-MOF-74[41]	4.34	3.20	74	41	84
Co-carborane MOF-4b[66]	0.07	0.06	84	154	104
rGA	0.14	0.13	93	39	175
CNA	0.43	0.42	98	113	427

^{a} N_1^{ads} (mmol g^{-1}): CO$_2$ uptake under adsorption conditions. $\Delta N_1 = N_1^{ads} - N_1^{des}$ (mmol g^{-1}): working CO$_2$ capacity. $R = (\Delta N_1 / N_1^{ads}) \times 100$ (%): regenerability. $\alpha_{12}^{ads} = (N_1^{ads}/N_2^{ads})(y_2/y_1)$: selectivity under ambient adsorption conditions. $S = (\alpha_{12}^{ads})^2/(\alpha_{12}^{des})(\Delta N_1/\Delta N_2)$: sorbent selection parameter. 1: strongly adsorbed component (CO$_2$). 2: weakly adsorbed component (N$_2$). y: molar fraction in the equilibrium gas phase.

regenerability (R), adsorption selectivity (α_{12}^{ads}), and sorbent selection parameter (S) of well-known benchmark materials along with CNA and rGA itself are estimated under vacuum swing adsorption conditions (Table 1). These evaluation parameters and benchmark materials are adapted and chosen from precedent literature as a reasonable CO$_2$ adsorption evaluation standard.[39−42] The adsorption condition is assumed to be a CO$_2$/N$_2$ mixture in a 10:90 ratio to represent typical flue gas composition and to evaluate CNA in comparison with other benchmark materials under the same conditions.[42] CNA shows a moderate N_1^{ads} value of 0.43 mmol·g^{-1} compared to strong binding adsorbents, such as Zeolite-5A[6] (3.50 mmol·g-1), Zeolite-13X[7] (2.49 mmol·g^{-1}), and Ni-MOF-74[41] (4.34 mmol·g^{-1}). It is noteworthy that VSA conditions are chosen to directly compare the adsorption capacity of CNA with other benchmark materials, but CNA is expected to be a stronger competitor for higher pressure range where carbonaceous materials are at an advantage as indicated by superior CO$_2$ uptake of 4.2 mmol·g^{-1} at 1 bar.

The effective CO$_2$ adsorption of CNA at low pressure (0.1 bar) with moderate adsorption strength is beneficial for facile regeneration by pressure driven CO$_2$ adsorption/desorption (vacuum swing adsorption). Working capacity (ΔN_1), net amount of CO$_2$ release after adsorption, and regenerability (R), the percentage of reusable CO$_2$ capture site, reflect this aspect. Adsorbents with strong chemisorption sites generally suffer from largely diminished working capacity with respect to initial adsorption capacity, as demonstrated in Zeolite-13X (1.35 mmol·g^{-1}/2.49 mmol·g^{-1}), Zeolite-5A (2.36 mmol·g^{-1}/3.50 mmol·g^{-1}), and Ni-MOF-74 (3.20 mmol·g^{-1}/4.34 mmol·g^{-1}). By contrast, mild adsorbents such as ZIF-78 (0.58 mmol·g^{-1}/0.60 mmol·g^{-1}) and CNA (0.42 mmol·g^{-1}/0.43 mmol·g^{-1}) show minor reduction of working capacity with an excellent regenerability of 97.6%. The CO$_2$ adsorption/desorption

isotherms for repeated cycles (Figure 3b) also show excellent regenerability through multiple cycles. As displayed in Figure 3c, CO$_2$ adsorption shows a modest S-shaped isotherm, which is originated from strong CO$_2$−CO$_2$ interactions due to large quadrupole moment of CO$_2$.[43] However, N$_2$ adsorption shows a linear isotherm with minor uptakes. Interestingly, unlike other moderate binding adsorbents such as ZIF-78, CNA exhibits highly selective CO$_2$ adsorption against abundant N$_2$, as demonstrated by selectivity parameter (α_{12}^{ads}) and experimental adsorption result (Figure 3c). CO$_2$ and N$_2$ adsorption/desorption isotherms at 300 K reveals an outstanding selectivity value of 113. It is noteworthy that the metal-free CNA system displays equivalent or even higher selectivity over other candidates. Eventually, the sorbent selection parameter (S) is the key criterion, which sums up all aspects of adsorption/desorption capacity and selectivity and represents overall performance of adsorbent. CNA shows the excellent S value of 427 which is far greater than pristine reduced graphene oxide aerogel ($S = 175$). This indicates significant role of carbon nitride on CO$_2$ capture efficiency. It is noteworthy that some of benchmark materials with remarkably high adsorption capacity (zeolite series and Ni-MOF-74) show relatively lower S value than CNA due to the penalties in regenerability and selectivity parameter. Sorbent selection parameter is not the ultimate figure of merit for CO$_2$ capture efficiency, but this result illustrate the great advantages of carbon nitride adsorbent for CO$_2$ capture, particularly in terms of regenerability and selectivity, which rarely coexist.

Modeling Study of CNA through Density Functional Theory Calculation. To elucidate the microscopic origin of enhanced CO$_2$ adsorption and selectivity of carbon nitride, we performed first-principles density functional theory (DFT) calculations on carbon nitride model in parallel with graphene as the reference. The difference in adsorption mechanisms is elucidated between graphene and carbon nitride, the latter of which is largely governed by the distinctive nonplanar porous geometry. At pristine graphene surface, CO$_2$ and N$_2$ adapt substrate-parallel adsorption configuration to maximize van der Waals contact surface. Three unique binding sites were identified, including (i) hexagonal center, (ii) above carbon atom, and (iii) above C−C bond center (Supporting Information, S Figure 7). The optimized geometries of adsorbed molecules reveal typical van der Waals distances of 3.2−3.5 Å. Owing to the larger van der Waals contact area, CO$_2$ has slightly stronger adsorption energies than N$_2$. For all three different binding sites, the standard deviation of adsorption energies is negligible. This clarifies that the local surface geometry of graphene does not significantly influence the adsorption strength. Overall, the interaction between CO$_2$/N$_2$ and pristine graphene surface is pure van der Waals type relying on the $\pi-\pi$ stacking interaction between π orbitals of CO$_2$/N$_2$ and π network of graphene.
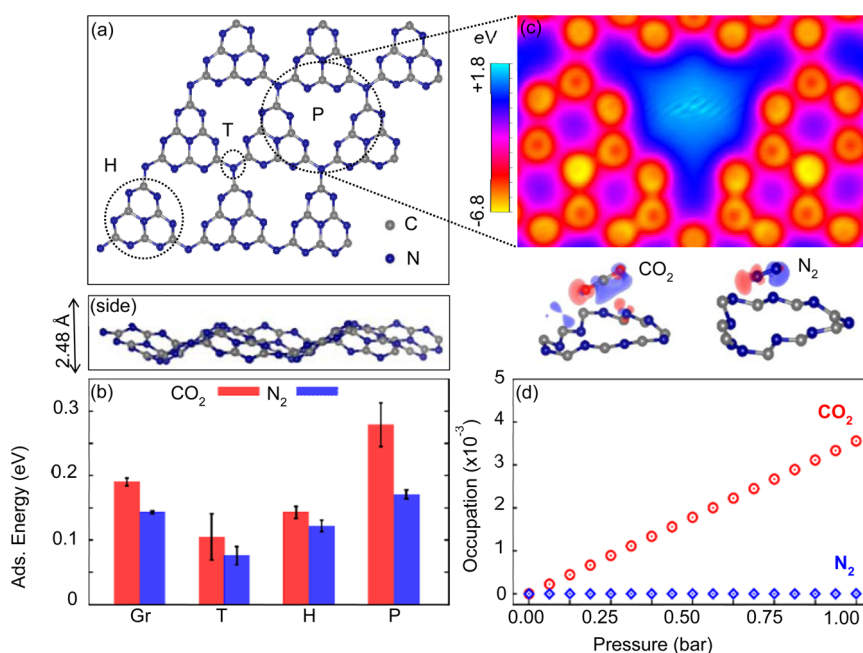
Figure 4. (a) DFT analysis of gas adsorption. (a) Optimized geometry of heptazine-based g-C_3N_4 (top and side view). The corrugation is shown in the unit of Å. (b) Averaged DFT adsorption energies of single CO_2/N_2 at the pore site (P), heptazine (H) and tertiary N (T), in comparison with pristine graphene (Gr). The error bars represent standard deviation from mean adsorption energies. (c) Contour plot of average electrostatic potential of g-C_3N_4, representing electron distribution at the pore site. The differential charge density map of captured CO_2/N_2 indicates polarization of CO_2/N_2 via dipole-induced dipole interaction. The blue and red colors represent the charge depletion and accumulation, respectively. (d) Estimated CO_2/N_2 occupation number as a function of the total pressure (10% CO_2 and 90% N_2), following first-principles thermodynamics and grand canonical ensemble formalism.

The typical adsorption sites for graphitic carbon nitride were classified into (i) tertiary N site, (ii) heptazine site, and (iii) pore site (Figure 4a). For each adsorption site, adsorption energies (E_{ads}) of a single CO_2/N_2 molecule were averaged over nine distinct possible configurations. Interestingly, the standard deviations in averaged E_{ads} exhibit the strong correlation with surface geometry of nonplanar porous carbon nitride. From a structural viewpoint, graphitic carbon nitride is constructed from two-dimensionally interconnected heptazine units solely through N linkages.[44] This framework puts forward a unique feature with both high porosity and mechanical flexibility. The obtained standard deviations serve as an indication of directional dependence of CO_2/N_2 adsorption on the g-C_3N_4 surface.

The tertiary N reveals noticeably weakened CO_2 affinity compared to pristine graphene. The limited van der Waals contact areas renders the tertiary N sites unfavorable sites for CO_2 (Figure 4b). The heptazine site is more rigid, resembling the surface of pristine graphene the most. However, the π network of the heptazine site is hampered by twisted geometry, favoring CO_2/N_2 head-on configuration with minimal strain (Figure 4b). By contrast, the pore sites demonstrate a noticeable enhancement in CO_2 capture and selectivity (Figure 4b). The electrostatic potential map (Figure 4c) shows the significant localization of electrons at N atoms, especially at the edges of the pore

sites. The electron-rich N atoms may polarize CO_2/N_2 molecules, leading to an enhanced adsorption by induced dipole–dipole interaction. The magnitude of binding energy (0.27 eV) for CO_2 is ideally in the optimum level for facile reversible adsorption/desorption (Figure 4d). We note that the differential charge density plots of CO_2 adsorption at tertiary-N and heptazine sites reveal little or no polarization effect (Supporting Information, S Figure 8). Here, the arrangement of pore edges mitigate steric repulsion and play a key role in the effective polarization of CO_2/N_2 molecules (Figure 4c). The average surface roughness of g-C_3N_4 arising from nonplanar nitrogen bond angles was calculated to be 0.57 ± 0.41 Å. The local geometry of the pore always consists of concave-up and concave-down edges, exposing the electron-rich edges toward gas molecules (Figure 4c). These polarizable edges slightly bend (2.07°) the adsorbed CO_2 molecule at the pore site, indicating the involvement of enhanced physisorption mechanics. Indeed, CO_2 molecule possesses a higher quadrupole moment and polarizability than N_2.[45] For all adsorption configurations, our DFT adsorption energies show preference of CO_2 over N_2 (Figure 4b). Whether the intrinsic difference in electronic structures can amount to a meaningful selectivity at ambient condition is the key of our proposal. By employing the intrinsic corrugated geometry of g-C_3N_4 with direct exposure of polarizing edges, we can capitalize on the aforementioned intrinsic polarizability of CO_2. In addition, no significant change in

geometry or electronic properties of carbon nitride has been observed since the interaction nature with CO_2/N_2 falls within the physisorption regime.

To illustrate the influence from polarizable edges of carbon nitride pores on the adsorption/desorption thermodynamics, we calculate the occupation number of adsorbed gas molecules at the pore site using first-principles thermodynamics,[46] represented by the differential Gibbs free energy $\Delta G(T,P)$ and grand canonical ensemble approach.[47] As the possible occupation numbers are either 0 (desorption) or 1 (adsorption) at the pore site, the average occupation number f is represented by

$$f = \frac{e^{-\Delta G/k_B T}}{1 + e^{-\Delta G/k_B T}}$$

First-principles $\Delta G(T,P)$ was obtained from the adsorption energy, zero-point energy, vibrational entropy, and finite-temperature chemical potential of CO_2 and N_2. The calculated occupation number at the experimental gas composition of 10% CO_2 and 90% N_2 at 300 K (Figure 4d) shows a remarkable agreement with experimental observation (Figure 3c). This verifies that the high CO_2/N_2 selectivity originates from the polarizing carbon nitride edges even at ambient condition. The polarity driven selectivity enhancement strategy is effective not only for metal-based adsorbents like MOF,[48−50] but also for nonmetal adsorbent like the case of CNA.

CONCLUSION

We have demonstrated the CO_2 capture of metal-free large surface area carbon nitride heterostructure in a highly regenerative and selective manner. Template growth of carbon nitride on porous reduced graphene oxide grants readily accessible CO_2 capture site and volumetric space for reserving incoming gas without serious chemical modification of carbon nitride. Strong dipole interaction induced by electron-rich nitrogen at nonplanar microporous carbon nitride geometry enforces specific and reversible adsorption of CO_2 under ambient condition. Thus, the possible CO_2 capture by pressure swing grants energy-efficient, economical, and sustainable industrial flue gas treatment platform. Judicious utilization of the well-balanced and specific binding at layered materials would also be useful for photocatalysis,[51] sensory, natural gas processing,[52] biomolecule imaging,[53] CO_2 capture,[54] and so on. Besides, effective enlargement of functional layered material surface by template growth at reduced graphene oxide surface may be applicable to other carbon nanostructure (e.g., CNT) and broaden the functionality of carbonaceous materials.

METHODS

Synthesis of Graphene Oxide. Graphite (1 g; flakes, + 100 mesh, Sigma-Aldrich), $NaNO_3$ (1 g; ≥99.0%, Sigma-Aldrich), and sulfuric acid (47 mL; ACS reagent, 95.0−98.0%, Sigma-Aldrich) were added to a round-bottom flask and mixed with a stirring bar. $KMnO_4$ (Powder, 97%, Sigma-Aldrich) was slowly added to the flask where an ice bath was placed at the bottom of the flask to keep the temperature low during the addition. The mixture solution was kept at 35 °C for 2 h with continuous stirring. The flask was cooled with an ice bath while 20 mL of H_2O_2 (reagent, 30%, JUNSEI) was added slowly with stirring for 30 min. The resulting solution was filtered and washed with 4% HCl five times. The filtered solid was dried under vacuum for 24 h at room temperature. Every 1 g of graphene oxide solid was mixed with 500 mL of deionized water and sonicated for 2 h. The sonicated GO suspension was centrifuged at 1500−2000 rpm for 40 min to isolate exfoliated GO from the rough graphite residue. The exfoliated GO solution was purified with a dialysis tube for 2 weeks where fresh deionized water was supplied every 24 h.

Synthesis of Dicyandiamide-Functionalized Reduced Graphene Oxide Aerogel (D-rGA). L-Ascorbic acid (0.1 g) and varying amounts of dicyanamide (40−400 mg) were added to 5 mL of exfoliated graphene oxide solution (2.4 mg·mL^{-1}) and heated with stirring at 50 °C for 30 min. The resulting black solution was cooled to room temperature, and slow gelation occurred within 8−10 h, turning the viscous solution into a monolithic gel. There is a practical limit in the N-content (<10 wt %) in the gel network structure due to the unstable solidification of graphene gel with dicyandiamide concentrations higher than 40 mg·mL^{-1}. This gel was first washed with hot H_2O twice and then submerged with H_2O for 5 d and ethanol for 5 d, consecutively. Every 8 h, submerging solvent medium was exchanged with fresh medium to wash out remaining ionic precursors or byproducts. Solvent-exchanged gel is dried with CO_2 at supercritical point. The resulting gel turns into a flexible and monolithic aerogel.

Thermal Treatment and Synthesis of Carbon Nitride Functionalized Aerogel (CNA). The monolithic D-rGA sample was placed inside of a ceramic crucible and heated in the tubular furnace under nitrogen atmosphere at 200 °C for 2 h. The ramping rate was set to 5 °C/min, and cooling was performed at room temperature quenching.

Porosimetry Analysis. Detailed analysis of porous structures was determined through nitrogen and argon adsorption/desorption isotherm. Micromeritics ASAP 2020 was used for both N_2 and Ar isotherm measurement. Brunauer−Emmett−Teller (BET) and Horvath−Kawazoe (HK) models were used to evaluate surface area and pore size distribution, respectively.

Characterizations. FT-IR spectroscopy was measured using Bruker IF66/S and Hyperioin 3000 with attenuated total reflectance (ATR) mode between 600 and 4000 cm^{-1}. Powder X-ray diffraction (PXRD) analysis was performed using Rigaku D/MAX-2500 (18 kW) within 3−60° range, 2°/min scan speed, and 40 kV 300 mA. X-ray photoelectron spectroscopy (XPS) measurement was performed using Thermo VG Scientific Sigma Probe. The CHN element was analyzed using a Thermo Scientific Flash 2000 analyzer. Scanning electron microscope (SEM) images were taken using FEI Magellan 400 with 1−5 kV power, 13 pA to 1.6 nA current, and 500×−100000× magnification mode. Transmission electron microscope (TEM) images were captured using FEI Tecnai G2 F30. Thermal gravimetric analysis was performed by Setaram Setsys 16/18 at 25−600 °C in N_2 atmosphere.

CO_2 and N_2 Adsorption analysis. Before the gas adsorption measurement, rGO aerogel samples were dried under vacuum at 200 °C for 24 h. For gas adsorption, Micromeritics ASAP 2020 was used to evaluate how effective these rGO aerogel samples can adsorb CO_2 gas in comparison with N_2 gas. CO_2 and N_2 gas adsorption/desorption isotherms were measured in the range of 0−1 bar at 300 K separately. For regenerability evaluation experiments, multiple runs of CO_2 adsorption isotherm were measured without degassing process before the analysis.

Gas Capture Efficiency Evaluation Criteria. To evaluate how efficiently material can capture CO_2 in flue gas conditions, we

assumed that CO_2 is present as 10% in the mixture form with N_2 as 90%. The rest of the real flue gas components such Ar, NO_x, SO_2, and others were excluded to simplify the evaluation. Five adsorbent evaluation criteria were adopted[42] and used herein to assess CO_2 capture capability in comparison with previously reported benchmark materials (e.g., zeolites, and MOFs). For evaluation of these parameters, individual N_2 and CO_2 isotherms of samples are measured at 300 K. These are CO_2 adsorption capacity ($N_1^{ads}[mmol \cdot g^{-1}]$), working CO_2 capacity ($\Delta N_1 = N_1^{ads} - N_1^{des}[mmol \cdot g^{-1}]$), regenerability ($R = (\Delta N_1/N_1^{ads}) \times 100$ (%)), adsorption selectivity ($\alpha_{12}^{ads} = (N_1^{ads}/N_2^{ads})(y_2/y_1)$), and sorbent selection parameter ($S = ((\alpha_{12}^{ads})^2/(\alpha_{12}^{des})) \cdot (\Delta N_1/\Delta N_2)$). CO_2 adsorption capacity means how much volume of CO_2 can be loaded into a given weight of material. Working capacity indicates the net adsorption capacity which can be found from the difference between the adsorbed amounts at the adsorption pressure (0.1 bar for CO_2 and 0.9 bar for N_2) and desorption pressure (0.01 bar for CO_2 and 0.09 bar for N_2). The adsorption pressure and desorption pressure are assumed if flue gas is released at 1 bar with a CO_2/$N_2 = 1$:9 ratio and adsorbed at 1 bar and desorbed through the vacuum swing process at 0.1 bar. Regenerability measures reusability of materials, and selectivity indicates how material can selectively remove CO_2 over N_2. The sorbent selection parameter combines adsorption selectivity and working capacity to evaluate overall performance of given material. N stands for the amount of adsorption, subscripts 1 and 2 for strongly bound gas (CO_2) and weakly bound gas (N_2), respectively, and y for mole fraction.

Computational Methods. We employed the projector-augmented wave (PAW) potentials[55] with Perdew−Burke−Ernzenrhof (PBE) exchange-correlation functional[56] within density-functional theory (DFT) as implanted in the Vienna Ab-Initio Simulation Package (VASP).[57] The simulation cell of single-layer C_3N_4 (g-C_3N_4) corresponds to a $3 \times 3 \times 1$ supercell consisting of 126 atoms in total. The steric repulsion between dangling bonds at the edge of the pore facilitates a structure preference of the buckled geometry over the planar geometry as demonstrated in the previous experimental and theoretical studies.[58−60] Since the heptazine moieties are connected solely through tertiary N linkages, g-C_3N_4 is susceptible to adsorption-induced strains. Thus, the size of simulation cell was chosen to minimize the effect of strain on the calculated adsorption energies. The CO_2/N_2 adsorption characteristic of g-C_3N_4 was compared with a $6 \times 6 \times 1$ supercell of pristine graphene where the gas-substrate interaction is well established to be van der Waals physisorption.[61] A plane-wave basis set with an energy cutoff of 500 eV was chosen to ensure convergence of total energy within a few meV. We adopted $2 \times 2 \times 1$ k-points sampling for g-C_3N_4 and $3 \times 3 \times 1$ k-points sampling for the graphene supercell. All atomic forces were fully relaxed to less than 0.015 eV/Å. A 15-Å vacuum was imposed in all calculations to minimize any spurious image−image interaction. The adsorption energy (E_{ads}) of single gas molecules is formulated based on DFT total energies as follows

$$E_{ads} = E_{sub} + E_{gas} - E_{sub+gas}$$

where E_{sub}, E_{gas}, and $E_{sub+gas}$ are total energies of g-C_3N_4 substrate, CO_2/N_2 molecule, and gas-absorbed systems, respectively. We chose to adapt the convention in which positive adsorption energy ($E_{ads} > 0$) indicated a favorable interaction between gas molecule and substrate. To obtain more reliable adsorption energies in the physisorption regime, we also employed the van der Waals corrected DFT-D2 method readily implemented in VASP.[62,63] Since the adsorption−desorption thermodynamics of CO_2/N_2 is pressure dependent, the free energy change ΔG is more relevant to selectivity than the binding energy E_{ads}. Adopting our previous formalism, ΔG of adsorption can be decomposed as follows:[64]

$$\Delta G(T, P) = \Delta E + \Delta ZPE + \Delta F(T) - \mu_{gas}^o - k_B T \ln \frac{P}{P_0}$$

Here, the ΔG was calculated as G(adsorbed) − G(desorbed) in view of CO_2/N_2 adsorption. Then, $\Delta E = -E_{ads}$ as mentioned before. The zero-point energy correction (ΔZPE) and vibrational

free energy correction (ΔF) were obtained from DFT vibrational spectra. Standard CO_2/N_2 chemical potentials (μ_{gas}) were extracted from tabulated thermodynamic table. To obtain accurate vibration spectra, atomic geometries were tightly optimized until all forces were less than 10^{-3} eV/Å. Phonon calculations were carried out with a fixed displacement of 0.01 Å for atoms constituting the edge of g-C_3N_4. The average occupation numbers f of CO_2/N_2 were derived from the grand-canonical ensemble approach,[13] bounded by the desorption limit ($f = 0$) and the adsorption limit ($f = 1$).

$$f = \frac{e^{-\Delta G/k_B T}}{1 + e^{-\Delta G/k_B T}}$$

We now demonstrate that grand canonical ensemble is equivalent to the well-known Langmuir isotherm. First, the Boltzmann factor can be decomposed as follows:

$$e^{-\Delta G/k_B T} = e^{-\Delta E + \Delta ZPE + \Delta F - \mu_{gas}^o - k_B T \ln \frac{P}{P_0}/k_B T}$$

$$= e^{-\Delta E + \Delta ZPE + \Delta F/k_B T} e^{\mu_{gas}^0/k_B T} e^{\ln P/P_0}$$

The first exponent term denotes $\mathscr{Z}(T)$ the partition function of system. The adsorption−desorption equilibrium constant $\mathscr{K}(T)$ in the Langmuir isotherm is shown to have a simple microscopic interpretation related to $\mathscr{Z}(T)$:

$$f = \frac{e^{-\Delta G/k_B T}}{1 + e^{-\Delta G/k_B T}} = \frac{\mathscr{Z}(T)e^{\mu_{gas}^0/k_B T}P}{1 + \mathscr{Z}(T)e^{\mu_{gas}^0/k_B T}P} = \frac{\mathscr{K}(T)P}{1 + \mathscr{K}(T)P}$$

For CO_2 gas, E_{ads}, ΔZPE, ΔF, and μ_{gas} terms were calculated to be 0.295, 0.019, −0.206, and −0.568 eV, respectively. Likewise, the corresponding terms for N_2 gas were calculated to be 0.174, 0.019, −0.195, and −0.686 eV, respectively. In accordance with the experimental conditions, we have considered a flue gas mixture of 10% CO_2 and 90% N_2 with total pressures of 0.1 bar at the desorption limit and 1.0 bar at the adsorption limit. On the basis of these conditions, ΔG_{CO2} are 0.145 and 0.204 eV at the two operational limits, corresponding to occupation numbers of 3.61×10^{-3} and 3.68×10^{-4}, respectively. In contrast, ΔG_{N2} are evaluated to be 0.338 and 0.398 eV, resulting in much smaller occupation numbers of 2.04×10^{-6} and 1.99×10^{-7} at the two aforementioned conditions.

Conflict of Interest: The authors declare no competing financial interest.

Supporting Information Available: The Supporting Information is available free of charge on the ACS Publications website at DOI: 10.1021/acsnano.5b03400.

S Figures 1−8 and S Table 1 as described in the text (PDF)

Note Added after ASAP Publication: This paper published ASAP on August 19, 2015. An addition was made to the Acknowledgment section and the revised version was reposted on August 26, 2015.

REFERENCES AND NOTES

1. Olivier, J. G. J.; Janssens-Maenhout, G.; Muntean, M.; Peters, J. A. H. W. *Trends in Global CO_2 Emissions - 2013 Report*; PBL Netherlands Environmental Assessment Agency: The Hague, **2013**.

2. Rochelle, G. T. Amine Scrubbing for CO_2 Capture. *Science* **2009**, *325*, 1652–1654.

3. D'Alessandro, D. M.; Smit, B.; Long, J. R. Carbon Dioxide Capture: Prospects for New Materials. *Angew. Chem., Int. Ed.* **2010**, *49*, 6058–6082.

4. Haszeldine, R. S. Carbon Capture and Storage: How Green Can Black Be? *Science* **2009**, *325*, 1647–1652.

5. Metz, B.; Davidson, H.; de Coninck, H.; Loos, M.; Meyer, L. *Special Report on Carbon Dioxide Capture and Storage*; Cambridge University Press: Cambridge, **2005**.

6. Park, J. H.; Kim, J. N.; Cho, S. H.; Kim, J. D.; Yang, R. T. Adsorber Dynamics and Optimal Design of Layered Beds for Multicomponent Gas Adsorption. *Chem. Eng. Sci.* **1998**, *53*, 3951–3963.

7. Cavenati, S.; Grande, C. A.; Rodrigues, A. E. Adsorption Equilibrium of Methane, Carbon Dioxide, and Nitrogen on Zeolite 13X at High Pressures. *J. Chem. Eng. Data* **2004**, *49*, 1095–1101.

8. Wang, B.; Cote, A. P.; Furukawa, H.; O'Keeffe, M.; Yaghi, O. M. Colossal Cages in Zeolitic Imidazolate Frameworks As Selective Carbon Dioxide Reservoirs. *Nature* **2008**, *453*, 207–206.

9. Banerjee, R.; Phan, A.; Wang, B.; Knobler, C.; Furukawa, H.; O'Keeffe, M.; Yaghi, O. M. High-Throughput Synthesis of Zeolitic Imidazolate Frameworks and Application to CO_2 Capture. *Science* **2008**, *319*, 939–943.

10. Nugent, P.; Belmabkhout, Y.; Burd, S. D.; Cairns, A. J.; Luebke, R.; Forrest, K.; Pham, T.; Ma, S. Q.; Space, B.; Wojtas, L.; *et al.* Porous Materials with Optimal Adsorption Thermodynamics and Kinetics for CO_2 Separation. *Nature* **2013**, *495*, 80–84.

11. Britt, D.; Furukawa, H.; Wang, B.; Glover, T. G.; Yaghi, O. M. Highly Efficient Separation of Carbon Dioxide by a Metal-Organic Framework Replete with Open Metal Sites. *Proc. Natl. Acad. Sci. U. S. A.* **2009**, *106*, 20637–20640.

12. Demessence, A.; D'Alessandro, D. M.; Foo, M. L.; Long, J. R. Strong CO_2 Binding in a Water-Stable, Triazolate-Bridged Metal-Organic Framework Functionalized with Ethylene-diamine. *J. Am. Chem. Soc.* **2009**, *131*, 8784–8786.

13. Ferey, G. Hybrid Porous Solids: Past, Present, Future. *Chem. Soc. Rev.* **2008**, *37*, 191–214.

14. Zhang, Z.; Yao, Z.-Z.; Xiang, S.; Chen, B. Perspective of Microporous Metal-Organic Frameworks for CO_2 Capture and Separation. *Energy Environ. Sci.* **2014**, *7*, 2868–2899.

15. Lee, K.; Howe, J. D.; Lin, L.-C.; Smit, B.; Neaton, J. B. Small-Molecule Adsorption in Open-Site Metal−Organic Frame-works: A Systematic Density Functional Theory Study for Rational Design. *Chem. Mater.* **2015**, *27*, 668–678.

16. Yang, S.; Sun, J.; Ramirez-Cuesta, A. J.; Callear, S. K.; David, W. I. F.; Anderson, D. P.; Newby, R.; Blake, A. J.; Parker, J. E.; Tang, C. C.; *et al.* Selectivity and Direct Visualization of Carbon Dioxide and Sulfur Dioxide in a Decorated Porous Host. *Nat. Chem.* **2012**, *4*, 887–894.

17. Choi, H.; Park, Y. C.; Kim, Y.-H.; Lee, Y. S. Ambient Carbon Dioxide Capture by Boron-Rich Boron Nitride Nanotube. *J. Am. Chem. Soc.* **2011**, *133*, 2084–2087.

18. Kroke, E.; Schwarz, M. Novel Group 14 nitrides. *Coord. Chem. Rev.* **2004**, *248*, 493–532.

19. Wang, X. C.; Maeda, K.; Thomas, A.; Takanabe, K.; Xin, G.; Carlsson, J. M.; Domen, K.; Antonietti, M. A Metal-Free Polymeric Photocatalyst for Hydrogen Production from Water under Visible Light. *Nat. Mater.* **2009**, *8*, 76–80.

20. Zhang, X. D.; Xie, X.; Wang, H.; Zhang, J. J.; Pan, B. C.; Xie, Y. Enhanced Photoresponsive Ultrathin Graphitic-Phase C_3N_4 Nanosheets for Bioimaging. *J. Am. Chem. Soc.* **2013**, *135*, 18–21.

21. Bai, X. D.; Zhong, D. Y.; Zhang, G. Y.; Ma, X. C.; Liu, S.; Wang, E. G.; Chen, Y.; Shaw, D. T. Hydrogen Storage in Carbon Nitride Nanobells. *Appl. Phys. Lett.* **2001**, *79*, 1552–1554.

22. Jun, Y. S.; Park, J.; Lee, S. U.; Thomas, A.; Hong, W. H.; Stucky, G. D. Three-Dimensional Macroscopic Assemblies of Low-Dimensional Carbon Nitrides for Enhanced Hydrogen Evolution. *Angew. Chem., Int. Ed.* **2013**, *52*, 11083–11087.

23. Goettmann, F.; Fischer, A.; Antonietti, M.; Thomas, A. Chemical Synthesis of Mesoporous Carbon Nitrides Using Hard Templates and Their Use as a Metal-Free Catalyst for Friedel-Crafts Reaction of Benzene. *Angew. Chem., Int. Ed.* **2006**, *45*, 4467–4471.

24. Yang, S.; Gong, Y.; Zhang, J.; Zhan, L.; Ma, L.; Fang, Z.; Vajtai, R.; Wang, X.; Ajayan, P. M. Exfoliated Graphitic Carbon Nitride Nanosheets As Efficient Catalysts for Hydrogen Evolution under Visible Light. *Adv. Mater.* **2013**, *25*, 2452–2456.

25. Zhang, Y. H.; Pan, Q. W.; Chai, G. Q.; Liang, M. R.; Dong, G. P.; Zhang, Q. Y.; Qiu, J. R. Synthesis and Luminescence Mechanism of Multicolor-Emitting g-C_3N_4 Nanopowders by Low Temperature Thermal Condensation of Melamine. *Sci. Rep.* **2013**, *3*, 1943.

26. Wang, Y.; Wang, X. C.; Antonietti, M. Polymeric Graphitic Carbon Nitride As a Heterogeneous Organocatalyst: From Photochemistry to Multipurpose Catalysis to Sustainable Chemistry. *Angew. Chem., Int. Ed.* **2012**, *51*, 68–89.

27. Teter, D. M.; Hemley, R. J. Low-Compressibility Carbon Nitrides. *Science* **1996**, *271*, 53–55.

28. Zhang, Y. J.; Fugane, K.; Mori, T.; Niu, L.; Ye, J. H. Wet Chemical Synthesis of Nitrogen-Doped Graphene towards Oxygen Reduction Electrocatalysts without High-Temperateure Pyrolysis. *J. Mater. Chem.* **2012**, *22*, 6575–6580.

29. Acik, M.; Lee, G.; Mattevi, C.; Chhowalla, M.; Cho, K.; Chabal, Y. J. Unusual Infrared-Absorption Mechanism in Thermally Reduced Graphene Oxide. *Nat. Mater.* **2010**, *9*, 840–845.

30. Hontoria-Lucas, C.; López-Peinado, A. J.; López-González, J. d. D.; Rojas-Cervantes, M. L.; Martín-Aranda, R. M. Study of Oxygen-Containing Groups in a Series of Graphite Oxides: Physical and Chemical Characterization. *Carbon* **1995**, *33*, 1585–1592.

31. Li, Y. G.; Zhang, J. A.; Wang, Q. S.; Jin, Y. X.; Huang, D. H.; Cui, Q. L.; Zou, G. T. Nitrogen-Rich Carbon Nitride Hollow Vessels: Synthesis, Characterization, and Their Properties. *J. Phys. Chem. B* **2010**, *114*, 9429–9434.

32. Maeda, K.; Wang, X. C.; Nishihara, Y.; Lu, D. L.; Antonietti, M.; Domen, K. Photocatalytic Activities of Graphitic Carbon Nitride Powder for Water Reduction and Oxidation Under Visible Light. *J. Phys. Chem. C* **2009**, *113*, 4940–4947.

33. Truica-Marasescu, F.; Wertheimer, M. R. Nitrogen-Rich Plasma-Polymer Films for Biomedical Applications. *Plasma Processes Polym.* **2008**, *5*, 44–57.

34. Graf, N.; Yegen, E.; Gross, T.; Lippitz, A.; Weigel, W.; Krakert, S.; Terfort, A.; Unger, W. E. S. XPS and NEXAFS Studies of Aliphatic and Aromatic Amine Species on Functionalized Surfaces. *Surf. Sci.* **2009**, *603*, 2849–2860.

35. Khabashesku, V. N.; Zimmerman, J. L.; Margrave, J. L. Powder Synthesis and Characterization of Amorphous Carbon Nitride. *Chem. Mater.* **2000**, *12*, 3264–3270.

36. Liang, J.; Du, X.; Gibson, C.; Du, X. W.; Qiao, S. Z. N-Doped Graphene Natively Grown on Hierarchical Ordered Porous Carbon for Enhanced Oxygen Reduction. *Adv. Mater.* **2013**, *25*, 6226–31.

37. Yin, S.; Goldovsky, Y.; Herzberg, M.; Liu, L.; Sun, H.; Zhang, Y.; Meng, F.; Cao, X.; Sun, D. D.; Chen, H.; *et al.* Porous Graphene: Functional Free-Standing Graphene Honeycomb Films. *Adv. Funct. Mater.* **2013**, *23*, 2971–2971.

38. Oh, J.; Lee, S.; Zhang, K.; Hwang, J. O.; Han, J.; Park, G.; Kim, S. O.; Park, J. H.; Park, S. Graphene Oxide-Assisted Produc-tion of Carbon Nitrides Using a Solution Process and Their Photocatalytic Activity. *Carbon* **2014**, *66*, 119–125.

39. Yang, R. T. *Fundamental Factors for Designing Adsorbent*; John Wiley & Sons, Inc.: New York, 2003; pp 8−16.

40. Rege, S. U.; Yang, R. T. A Simple Parameter for Selecting an Adsorbent for Gas Separation by Pressure Swing Adsorption. *Sep. Sci. Technol.* **2001**, *36*, 3355–3365.

41. Dietzel, P. D. C.; Besikiotis, V.; Blom, R. Application of Metal-Organic Frameworks with Coordinatively Unsaturated Metal Sites in Storage and Separation of Methane and Carbon Dioxide. *J. Mater. Chem.* **2009**, *19*, 7362–7370.

42. Bae, Y. S.; Snurr, R. Q. Development and Evaluation of Porous Materials for Carbon Dioxide Separation and Capture. *Angew. Chem., Int. Ed.* **2011**, *50*, 11586–11596.

43. Walton, K. S.; Millward, A. R.; Dubbeldam, D.; Frost, H.; Low, J. J.; Yaghi, O. M.; Snurr, R. Q. Understanding Inflec-tions and Steps in Carbon Dioxide Adsorption Isotherms in

Metal-Organic Frameworks. *J. Am. Chem. Soc.* **2008**, *130*, 406–407.

44. Jurgens, B.; Irran, E.; Senker, J.; Kroll, P.; Muller, H.; Schnick, W. Melem (2,5,8-triamino-tri-s-triazine), an Important Intermediate During Condensation of Melamine Rings to Graphitic Carbon Nitride: Synthesis, Structure Determination by X-ray Powder Diffractometry, Solid-State NMR, and Theoretical Studies. *J. Am. Chem. Soc.* **2003**, *125*, 10288–10300.

45. Bae, Y. S.; Lee, C. H. Sorption Kinetics of Eight Gases on a Carbon Molecular Sieve at Elevated Pressure. *Carbon* **2005**, *43*, 95–107.

46. Woo, S. J.; Lee, E. S.; Yoon, M.; Kim, Y. H. Finite-Temperature Hydrogen Adsorption and Desorption Thermodynamics Driven by Soft Vibration Modes. *Phys. Rev. Lett.* **2013**, *111*, 066102.

47. Lee, H.; Choi, W. I.; Ihm, J. Combinatorial Search for Optimal Hydrogen-Storage Nanomaterials Based on Polymers. *Phys. Rev. Lett.* **2006**, *97*, 056104.

48. Zhang, Z.; Li, Z.; Li, J. Computational Study of Adsorption and Separation of CO_2, CH_4, and N_2 by an Rht-Type Metal–Organic Framework. *Langmuir* **2012**, *28*, 12122–12133.

49. Wang, B.; Huang, H.; Lv, X.-L.; Xie, Y.; Li, M.; Li, J.-R. Tuning CO_2 Selective Adsorption over N_2 and CH_4 in UiO-67 Analogues Through Ligand Functionalization. *Inorg. Chem.* **2014**, *53*, 9254–9259.

50. Liang, Z.; Marshall, M.; Chaffee, A. L. CO_2 Adsorption-Based Separation by Metal Organic Framework (Cu-BTC) Versus Zeolite (13X). *Energy Fuels* **2009**, *23*, 2785–2789.

51. Cui, Y.; Ding, Z.; Fu, X.; Wang, X. Construction of Conjugated Carbon Nitride Nanoarchitectures in Solution at Low Temperatures for Photoredox Catalysis. *Angew. Chem., Int. Ed.* **2012**, *51*, 11814–11818.

52. Hwang, C.-C.; Tour, J. J.; Kittrell, C.; Espinal, L.; Alemany, L. B.; Tour, J. M. Capturing Carbon Dioxide As a Polymer from Natural Gas. *Nat. Commun.* **2014**, *5*. DOI: 10.1038/ncomms4961

53. Oh, J.; Yoo, R. J.; Kim, S. Y.; Lee, Y. J.; Kim, D. W.; Park, S. Oxidized Carbon Nitrides: Water-Dispersible, Atomically Thin Carbon Nitride-Based Nanodots and Their Performances as Bioimaging Probes. *Chem. - Eur. J.* **2015**, *21*, 6241–6246.

54. Oh, J.; Mo, Y.-H.; Le, V.-D.; Lee, S.; Han, J.; Park, G.; Kim, Y.-H.; Park, S.-E.; Park, S. Borane-Modified Graphene-Based Materials As CO_2 Adsorbents. *Carbon* **2014**, *79*, 450–456.

55. Blöchl, P. E. Projector Augmented-Wave Method. *Phys. Rev. B: Condens. Matter Mater. Phys.* **1994**, *50*, 17953.

56. Perdew, J. P.; Burke, K.; Ernzerhof, M. Generalized Gradient Approximation for The Exchange-Correlation Hole of a Many-Electron System. *Phys. Rev. Lett.* **1996**, *77*, 3865.

57. Kresse, G.; Joubert, D. From Ultrasoft Pseudopotentials to the Projector Augmented-Wave Method. *Phys. Rev. B: Condens. Matter Mater. Phys.* **1999**, *59*, 1758.

58. Deifallah, M.; McMillan, P. F.; Cora, F. Electronic and Structural Properties of Two-Dimensional Carbon Nitride Graphenes. *J. Phys. Chem. C* **2008**, *112*, 5447–5453.

59. Sehnert, J.; Baerwinkel, K.; Senker, J. *Ab Initio* Calculation of Solid-State NMR Spectra for Different Triazine and Heptazine Based Structure Proposals of g-C_3N_4. *J. Phys. Chem. B* **2007**, *111*, 10671–10680.

60. Tyborski, T.; Merschjann, C.; Orthmann, S.; Yang, F.; Lux-Steiner, M. C.; Schedel-Niedrig, T. Crystal Structure of Polymeric Carbon Nitride and the Determination of its Process-Temperature-Induced Modifications. *J. Phys.: Condens. Matter* **2013**, *25*, 395402.

61. Yim, W. L.; Byl, O.; Yates, J. T.; Johnson, J. K. Vibrational Behavior of Adsorbed CO_2 on Single-Walled Carbon Nanotubes. *J. Chem. Phys.* **2004**, *120*, 5377–5386.

62. Grimme, S. Semiempirical GGA-Type Density Functional Constructed with a Long-Range Dispersion Correction. *J. Comput. Chem.* **2006**, *27*, 1787–1799.

63. Kim, D. Y.; Lee, H. M.; Min, S. K.; Cho, Y.; Hwang, I. C.; Han, K.; Kim, J. Y.; Kim, K. S. CO_2 Capturing Mechanism in Aqueous Ammonia: NH_3-Driven Decomposition-Recombination Pathway. *J. Phys. Chem. Lett.* **2011**, *2*, 689–694.

64. Woo, S.-J.; Lee, E.-S.; Yoon, M.; Kim, Y.-H. Finite-Temperature Hydrogen Adsorption and Desorption Thermodynamics Driven by Soft Vibration Modes. *Phys. Rev. Lett.* **2013**, *111*. DOI: 10.1103/PhysRevLett.111.066102

65. Banerjee, R.; Furukawa, H.; Britt, D.; Knobler, C.; O'Keeffe, M.; Yaghi, O. M. Control of Pore Size and Functionality in Isoreticular Zeolitic Imidazolate Frameworks and Their Carbon Dioxide Selective Capture Properties. *J. Am. Chem. Soc.* **2009**, *131*, 3875–3877.

66. Bae, Y. S.; Spokoyny, A. M.; Farha, O. K.; Snurr, R. Q.; Hupp, J. T.; Mirkin, C. A. Separation of Gas Mixtures Using Co(II) Carborane-Based Porous Coordination Polymers. *Chem. Commun.* **2010**, *46*, 3478–3480.